Dynamic strain determination using fibre-optic cables allows imaging of seismological and structural features

Jousset et al.

Supplementary material

Supplementary Note 1 | Summary of the geology of Reykjanes peninsula, SW Iceland

The Reykjanes Peninsula is located at the tip of SW Iceland within the Western Volcanic Zone[1]. It is the on-shore prolongation of the Reykjanes Ridge (Northeast Atlantic Ocean). On Reykjanes, the extensional tectonic activity between the North American and Eurasian tectonic plates (2 cm/year, since 6-7 Ma) induce intense seismic activity associated with rifting processes with faults and several recent volcanic systems, with young and highly permeable basaltic formations of Pleistocene age. Tholeiitic basalts range from picrite basalts (oldest) to olivine tholeiites to tholeiites (youngest)[2]. Dike intrusions at depth provide the heat source for geothermal systems[3]. Some of those intrusions reach ground surface and produce eruptions in episodic intervals of roughly 1000 years. The most recent volcanic eruption on Reykjanes occurred as a row of scoria and spatter cones in 1210-1240 AD in the Svartsengi volcanic system (Eldvörp dyke). The Eldvörp crater row extends from the south coast about 10 km inland (Fig. 1). The lava emitted from the crater row is one of the most voluminous Holocene lava flows on the Reykjanes Peninsula, covering c. 20 km^2. Faults on Reykjanes are numerous and mostly exhibit normal mode, with sinistral shear components[4] due to the oblique character of the ridge compared to its opening in this area. Faults are partly covered by the most recent lava flows and have there no evident surface expression (Fig. 1).

Date	Time	Latitude	Longitude	Depth (km)	Ml
17.03.2015	123513.800	63.81570	-22.75730	-	-
	134329.595	63.88757	-22.07062	0.135	1.68
	141232.819	63.88997	-22.07200	0.135	2.07
	200757.138	63.91812	-21.16431	7.499	0.41
	232441.820	63.28078	-24.31998	10.005	1.97
	233444.400	63.82070	-22.75670	-	-
18.03.2015	012544.590	63.28132	-24.24640	10.005	2.41
	014237.490	63.26402	-24.17299	10.005	2.04
	021438.167	63.94202	-21.32619	5.553	1.11
	033632.982	63.60829	-23.83504	10.005	1.5
	040854.548	63.97064	-20.70711	7.071	0.81
	054525.347	63.97831	-20.92498	4.52	0.61
	062645.709	63.31213	-24.22322	10.005	1.62
	094803.941	63.94957	-21.04885	7.004	0.45
	110248.902	63.89518	-21.98165	7.688	0.4
	144059.750	63.94616	-21.34695	6.344	0.85
	152248.938	63.91788	-22.00966	8.244	1.03

	153855.951	63.91488	-22.01769	9.592	1.36
	155817.012	63.91555	-22.01686	8.52	1.02
19.03.2015	033544.069	63.85105	-22.41394	8.5	1
	062524.769	63.97066	-20.54266	6.85	1.26
	152428.448	63.62228	-23.48391	9.304	2.77
	152549.715	63.62851	-23.48808	9.701	3.52
	152809.069	63.62165	-23.49410	8.966	2.55
	153958.750	63.58426	-23.35005	2.423	1.94
	155620.472	63.60349	-23.29428	10.005	2.18
	160151.666	63.57256	-23.38467	10.005	2
	221122.717	63.93811	-21.07365	5.7	0.67
20.03.2015	000533.772	63.94842	-21.76611	8.974	0.86
	004942.159	63.95584	-20.23646	7.316	1.05
	190350.483	63.78902	-22.81958	7.743	1.46
21.03.2015	002505.530	63.72341	-23.08535	9.274	2.4
	005405.737	63.96001	-20.70190	5.956	0.35
	015441.493	63.74953	-23.04996	4.461	2.33
	015536.997	63.74246	-23.11171	11.35	2.14
	023719.045	63.72398	-22.99030	10.617	2.08
	023719.831	63.70922	-22.98475	10.059	2.14
	023808.480	63.75915	-23.11457	11.252	2.05
	023810.669	63.75466	-23.10264	11.774	2.56
	024404.898	63.73452	-23.09302	9.282	3.24
	025026.620	63.73301	-23.08797	10.417	2.28
	025452.008	63.74785	-23.07770	6.987	2.22
	031812.031	63.75742	-23.16852	8.602	1.65
	033104.042	63.78539	-22.98797	9.873	1.67
	033302.795	63.76807	-22.98377	5.032	1.87
	033306.076	63.75515	-23.04505	8.533	2.25
	033330.768	63.76606	-23.00832	2.616	2.21
	033538.282	63.73726	-23.05952	7.768	2.87
	033653.502	63.73884	-23.05099	10.165	1.99
	033926.265	63.74123	-23.06257	10.617	2.13
	035417.136	63.72586	-23.06321	7.942	2.46
	035458.362	63.72704	-23.08016	8.689	2.56
	051232.242	63.74422	-23.10125	9.838	1.29
	054840.536	63.74189	-23.09292	8.934	2.15
	060235.731	63.77201	-22.98975	10.64	1.72
	064316.494	63.74780	-23.12904	12.887	1.62
	071427.229	63.75529	-23.09480	11.416	2.1
	112237.699	63.73768	-23.09242	9.926	1.54
	194556.532	63.91367	-21.16575	6.05	0.28
	203339.304	63.93933	-21.38728	6.635	0.68
	212643.318	63.72953	-23.12332	11.88	2.29

22.03.2015	082045.522	63.95654	-21.14264	8.743	0.29
	111017.119	63.87780	-22.01269	6.608	0.36
	112257.624	63.98433	-20.70193	6.388	0.39
	192134.878	63.97046	-21.05165	4.913	0.26
	204902.766	63.92028	-21.26286	6.782	0.35
	211012.739	63.55810	-23.61405	10.005	2.19
	225140.600	63.84720	-22.68880	-	-
23.03.2015	160708.530	63.86623	-22.53574	3.563	1.4
24.03.2015	003113.952	63.97458	-20.70251	5.095	0.71
	061343.553	63.66073	-23.23991	13.204	1.83
	062926.968	63.63893	-23.29323	9.667	2.22
	063506.798	63.65860	-23.33569	11.436	1.65
	063710.401	63.67684	-23.32285	8.927	2.7
	064217.452	63.73769	-23.02685	13.117	2.04

Supplementary Table 1 | List of local earthquakes recorded during the DAS recording period

Date	Time (UTC)	Location	Depth (km)	Magnitude Mb	Distance to the fibre optic cable
17.03.2015	22:12:28	135 km NW of Kota Ternate	44	6.2	12,300 km
18.03.2015	18:27:29	75 km NNW from Talcahuano, Chile	13	6.2	12,000 km
23.03.2015	04:51:38	45 km ESE from Putre, Chile	130	6.4	10,000 km

Supplementary Table 2 | List of Teleseismic earthquakes during the DAS recording period

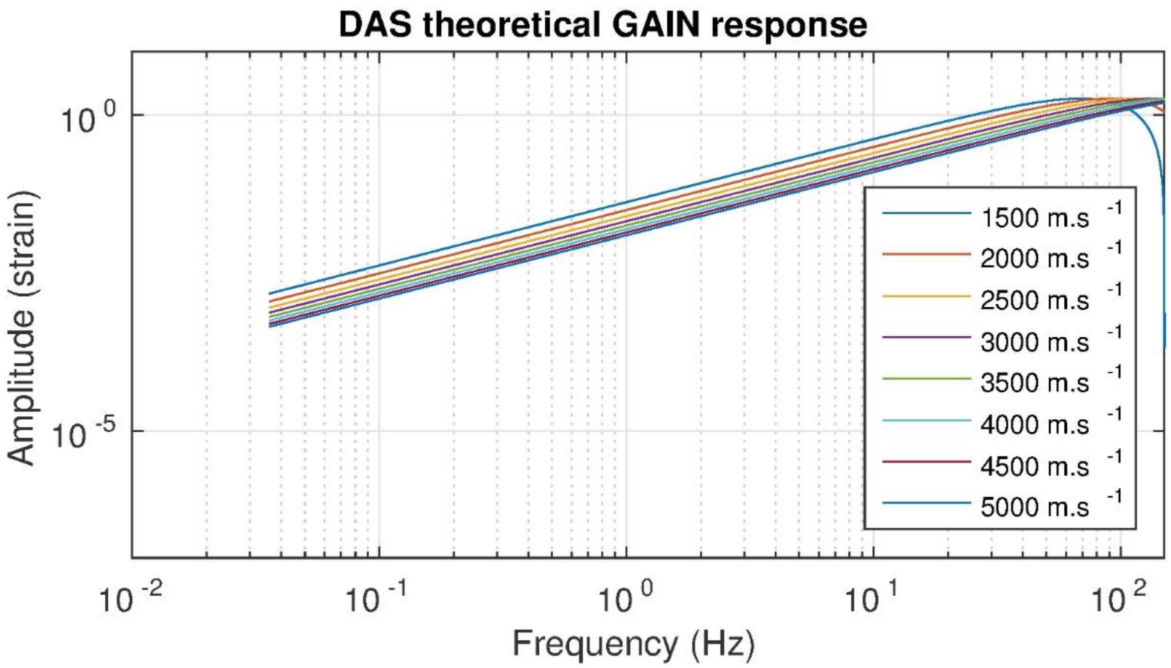

(a)

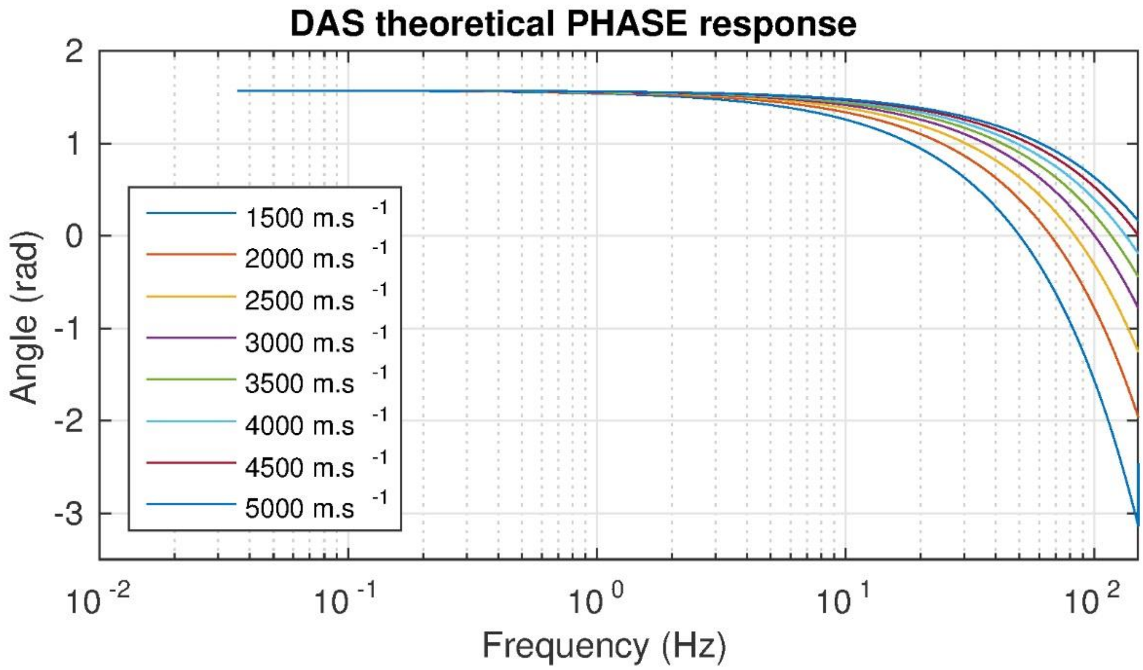

(b)

Supplementary Figure 1 | Theoretical instrumental response (in frequency) to an impulse in the time domain along the cable (incidence angle = 0; 10 m gauge length). The input signal is a propagating local displacement impulse of 1 nm magnitude along the cable. **a** amplitude; the amplitude output iDAS response is then expressed in strain (nm/m). **b** phase

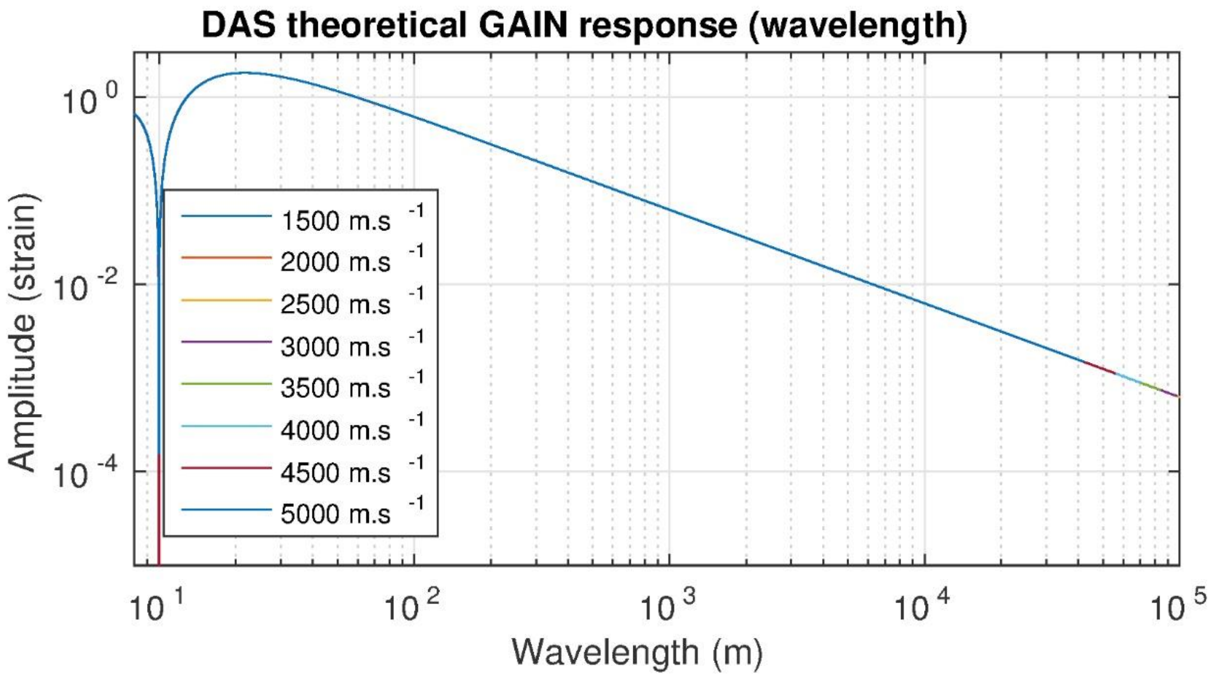

(a)

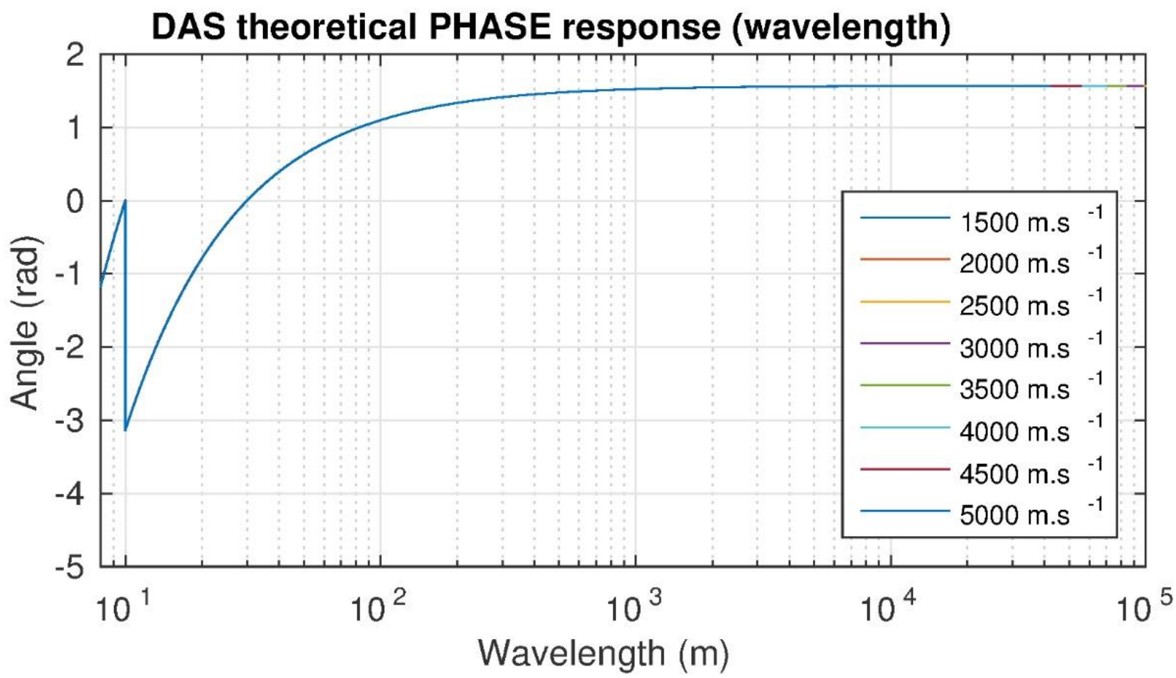

(b)

Supplementary Figure 2 | Theoretical instrumental response (in wavelength) to an impulse in the time domain along the cable (incidence angle = 0) expressed in wavelength. There is no dependency with the wave velocity. **a** amplitude. **b** phase

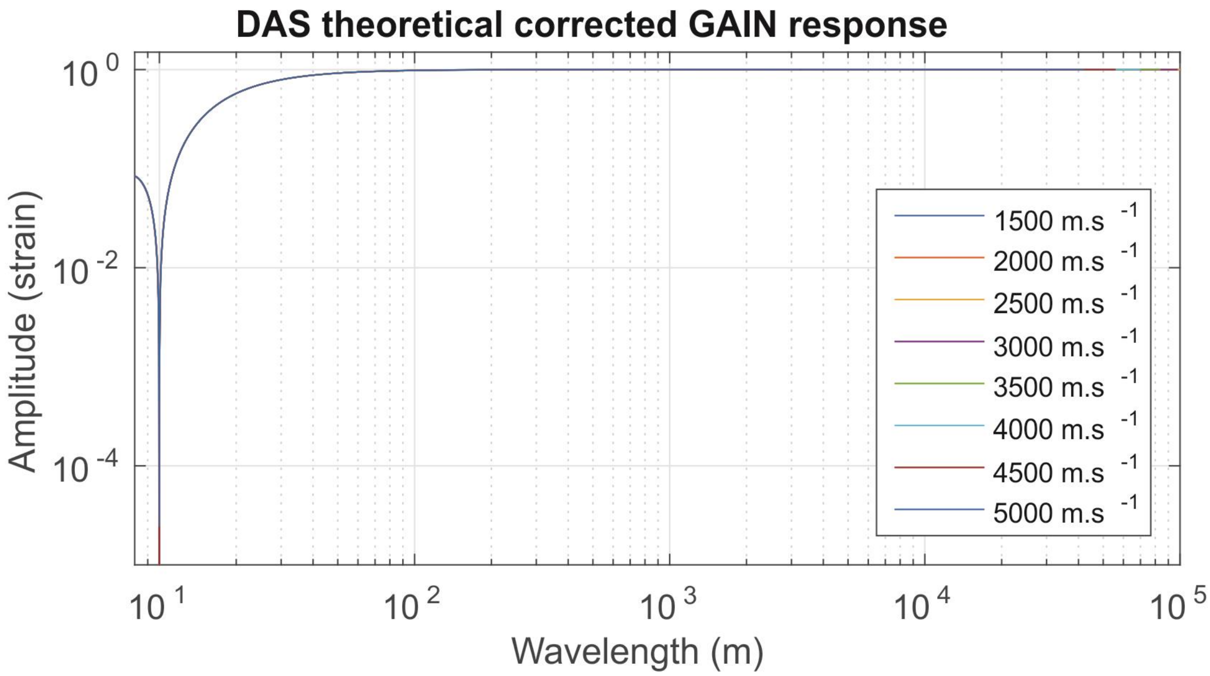

(a)

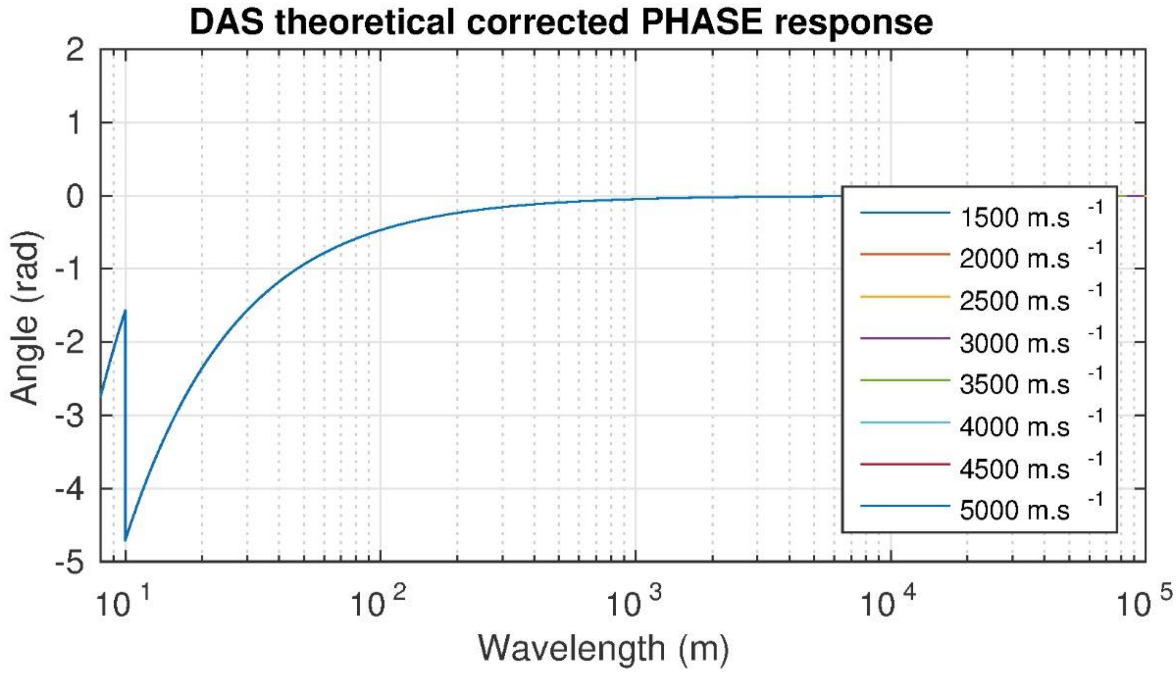

(b)

Supplementary Figure 3 | Theoretical instrumental response corrected from an approximation of the response for the long periods. The response is flat for wavelengths above 20 m, which is fine for seismic frequencies (< 100 Hz) at velocities above 1500 m/s. In the amplitude plot C=0.0159; in the phase plot the phase shift is π/2. **a** amplitude. **b** phase

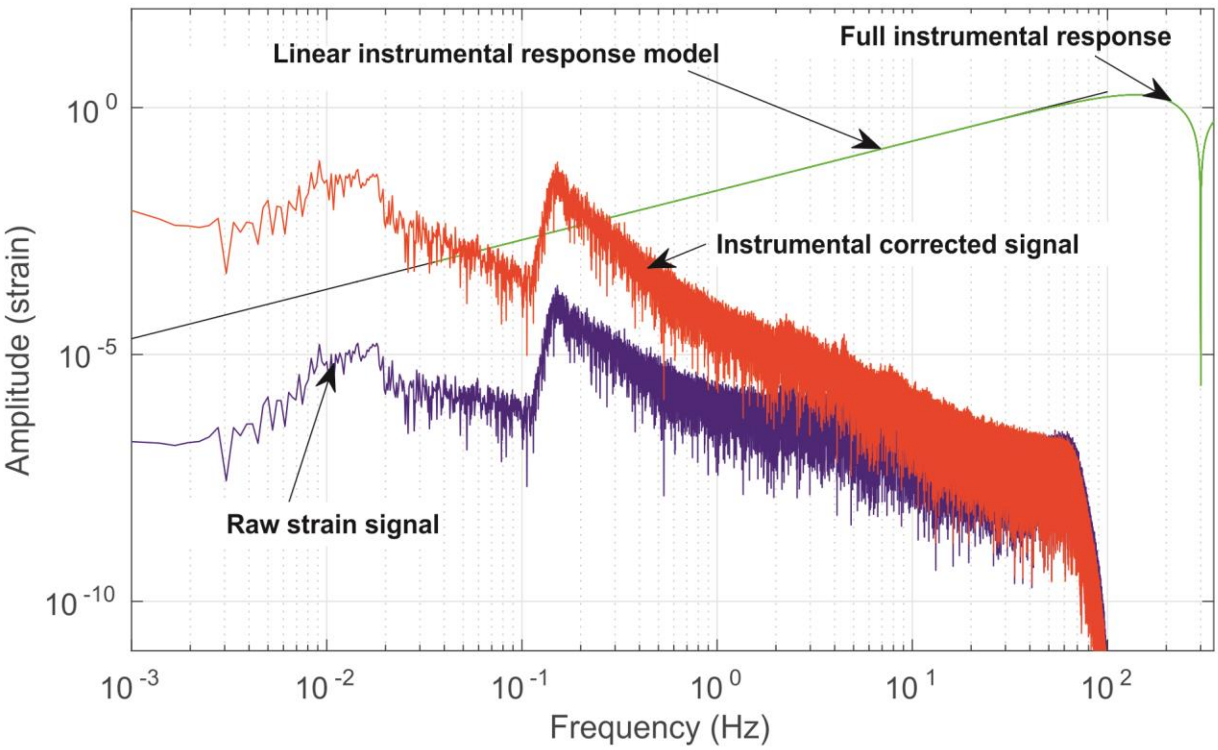

Supplementary Figure 4 | Restitution of the data by instrumental response correction

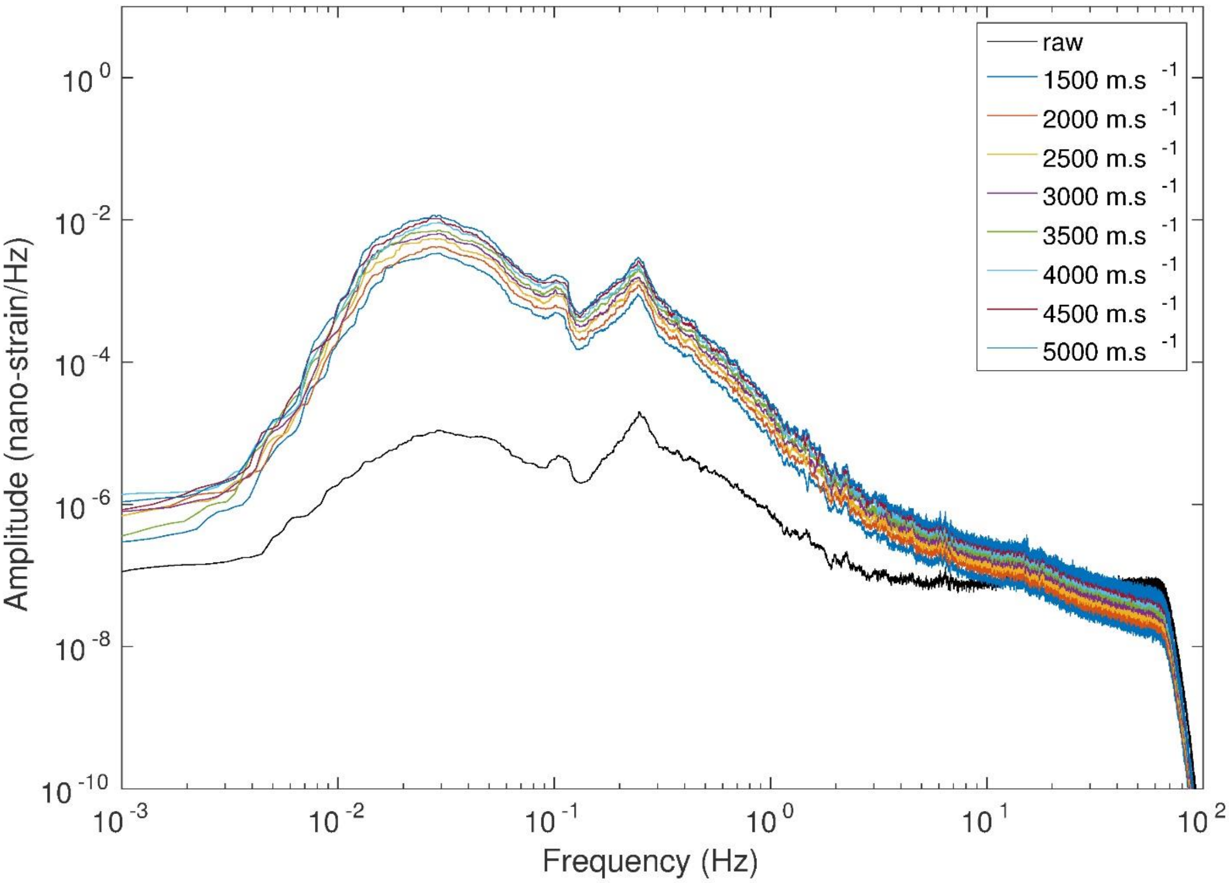

Supplementary Figure 5 | Restitution for various wave velocities

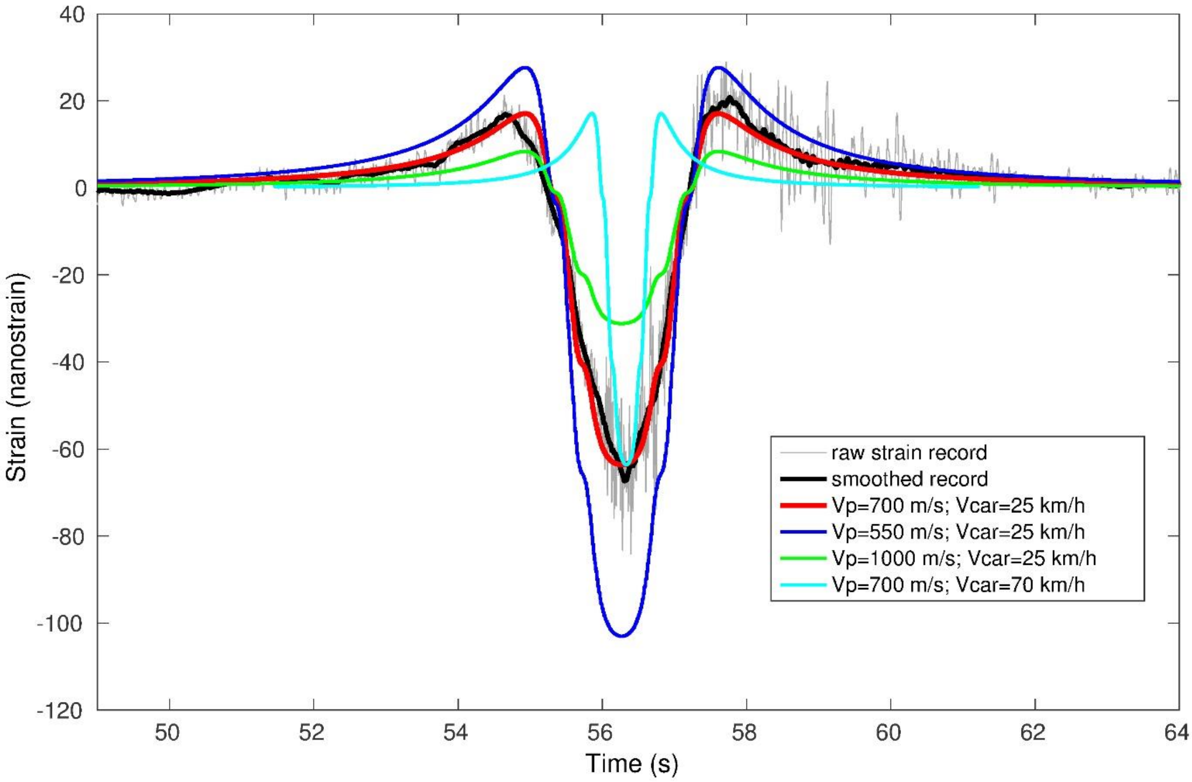

Supplementary Figure 6 | Deformation of the ground due to a ~2200 kg 4WD car on the ground surface

We model the weight of the car on the ground as the sum of 4 points load at the surface. The distance between the right and left wheels of the car is taken as~1.6 m and from the front and the rear wheels as ~2.8 m. We assume a ground density of 2000 $kg.m^{-3}$ and a Poisson ratio =0.25, typical values for basalts at the surface[4]. Grey light curve: recorded data. Thick black curve: same data but smoothed. Colour curves: modelled deformation for a car moving at different speed along a road for various P-wave ground velocities. The cable is assumed to be at 0.5 meter depth

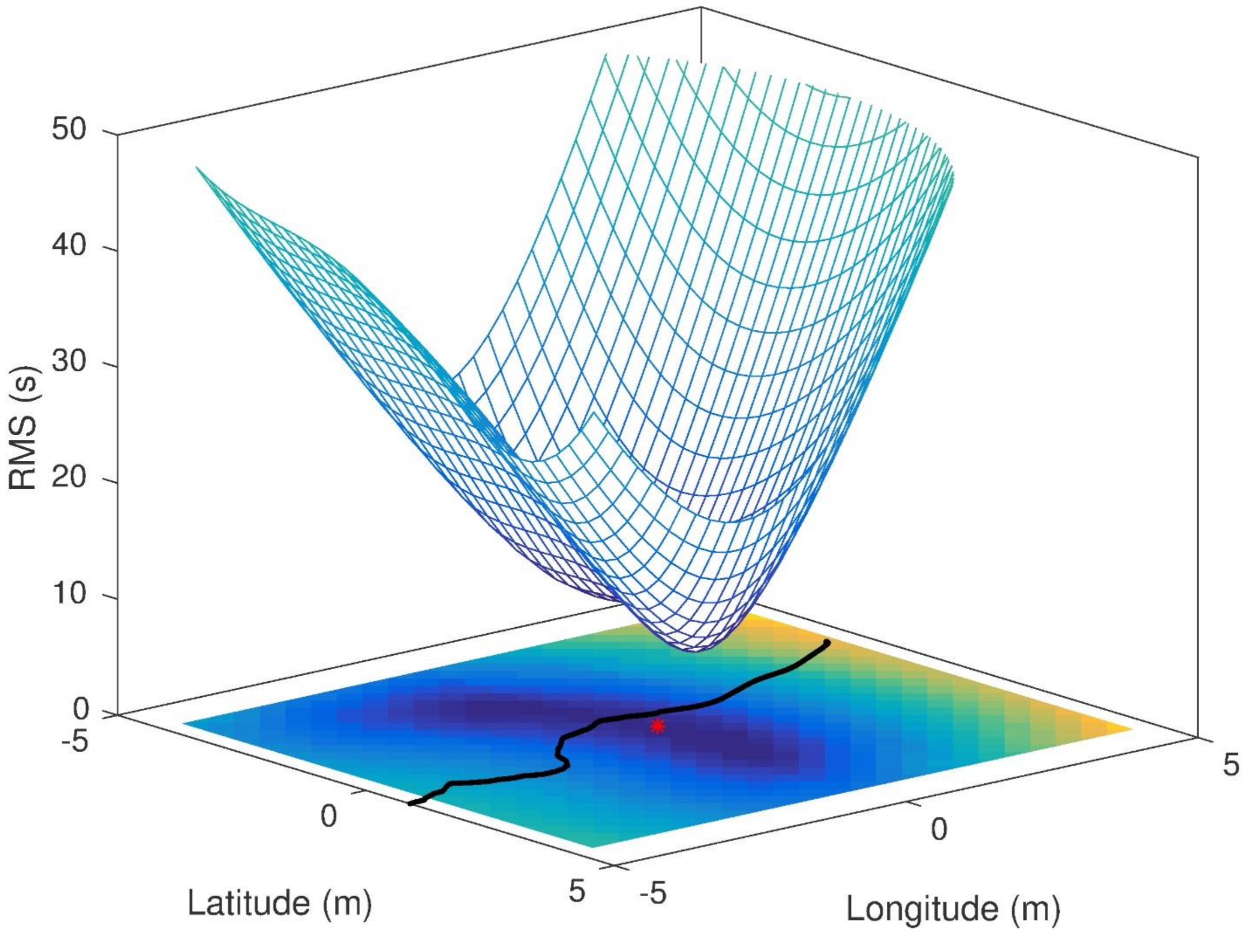

Supplementary Figure 7 | Probability density function of the hypocentre location determined with DAS data

We computed the probability density function using a grid search in a 3D grid with 10 km edge. When the hypothetic hypocentre is far from the true hypocentre location, the RMS value increases. When the hypothetic hypocentre is close to the true hypocentre, the RMS value decreases. The minimum value of the misfit is defined as the maximum probability of the hypothetical hypocentre to be at the true hypocentre location. The red star is the position of the hypocentre location defined by the travel time tomography. When projected on the base plane, the lowest values of the pdf (deep blue) encompass the most probable hypocentre location, similar to the hypocentre location found with the 3D tomographic inversion. The black line is the location of the fibre-optic cable. The inversion was performed with about 3000 P- and S- picks along the cable

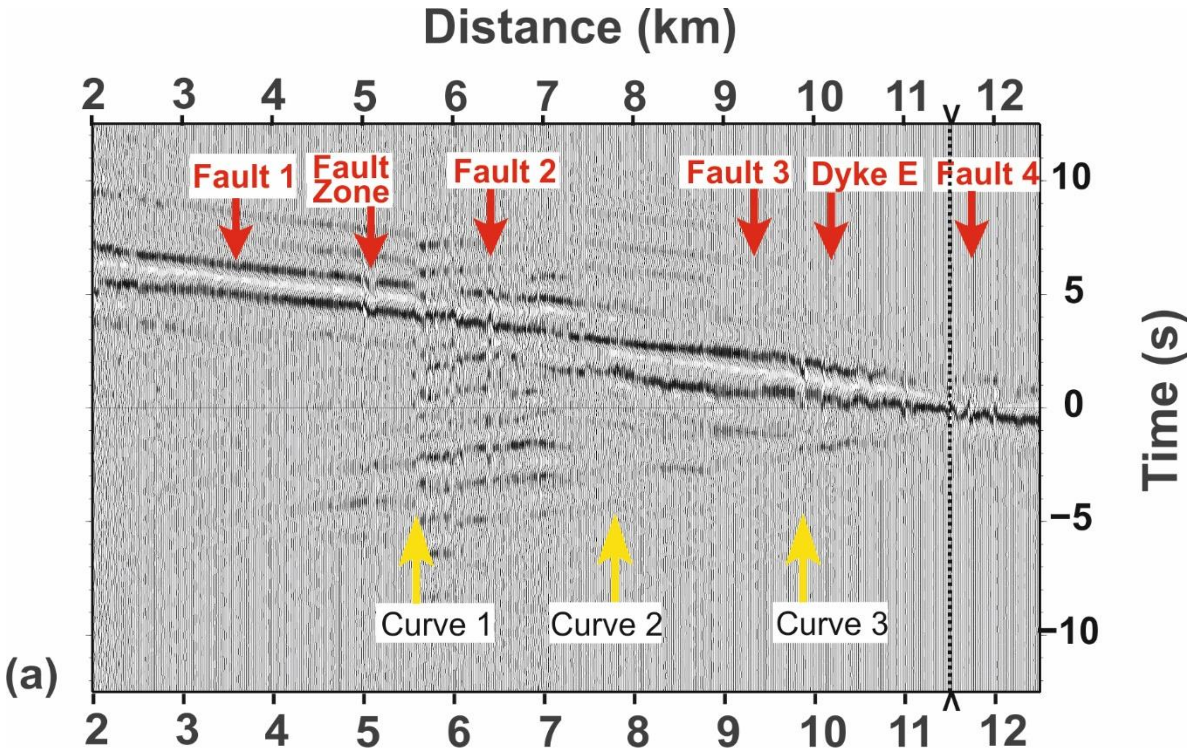
Distance (km)
2
3
4
5
6
7
8
9
10
11
12
Fault 1
Fault Zone
Fault 2
Fault 3
Dyke E
Fault 4
10
5
0
−5
−10
Time (s)
Curve 1
Curve 2
Curve 3
(a)

(a)

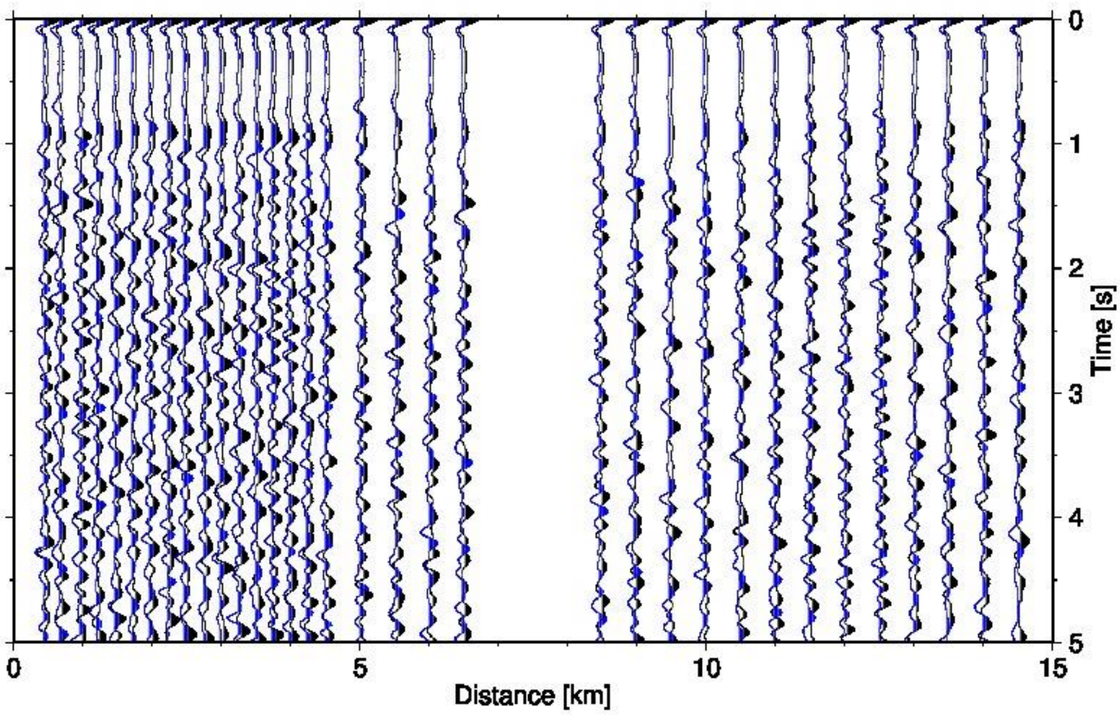
0
5
10
15
Distance [km]
0
1
2
3
4
5
Time [s]

(b)

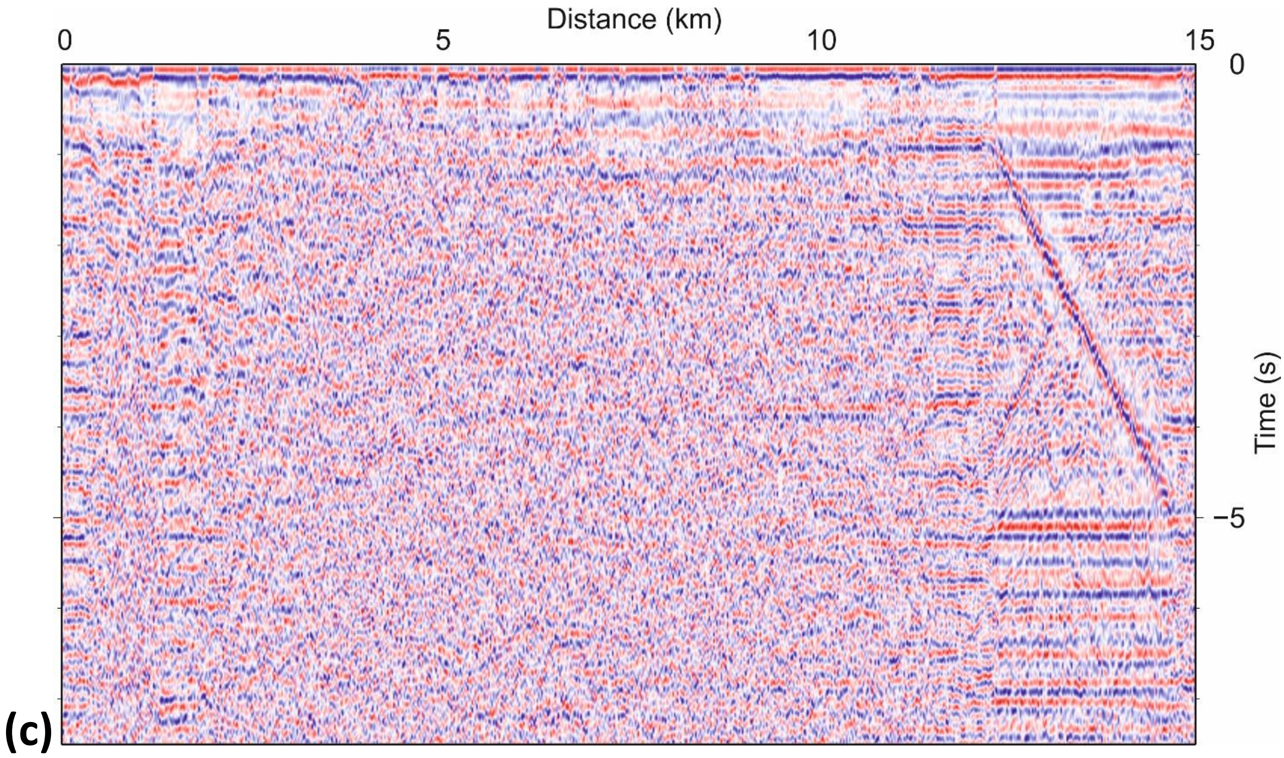

Supplementary Figure 8 | Ambient noise techniques results with DAS records.

a Ambient noise based, cross-correlation computed between all traces of the cable with respect to one arbitrary trace (at position ~11.5 km). The traces have been band-pass filtered between 0.5 and 2 Hz to enhance the Rayleigh waves. Note the perturbation of the wave field due to the presence of several geological features including a fault damage zone (FDZ) at ~5 km. **b** Autocorrelations computed for selected DAS/DVS traces (black) and for their closest geophones (blue) deployed along the cable (Fig. 1) showing that both sensors types led to comparative correlation results. Horizontal components of the geophones have been rotated into the direction along the optical cable. An automatic gain control (scaling in a moving window) with a window length of 1 second has been applied to suppress the strong arrival at 0 seconds. For clarity, the geophone traces have been shifted by few meters to the right. **c** Auto-correlation for all traces of the fibre optic cable, indicative for a highly complex, fine-scale structure below the fibre. Note a slight perturbation of the amplitudes in the image at the distance ~5 km, corresponding to the position of the fault damage zone and at ~10 km corresponding to the location of a dike. Beyond distance ~12 km, strong man-made noise (pipeline) dominates the autocorrelation signal

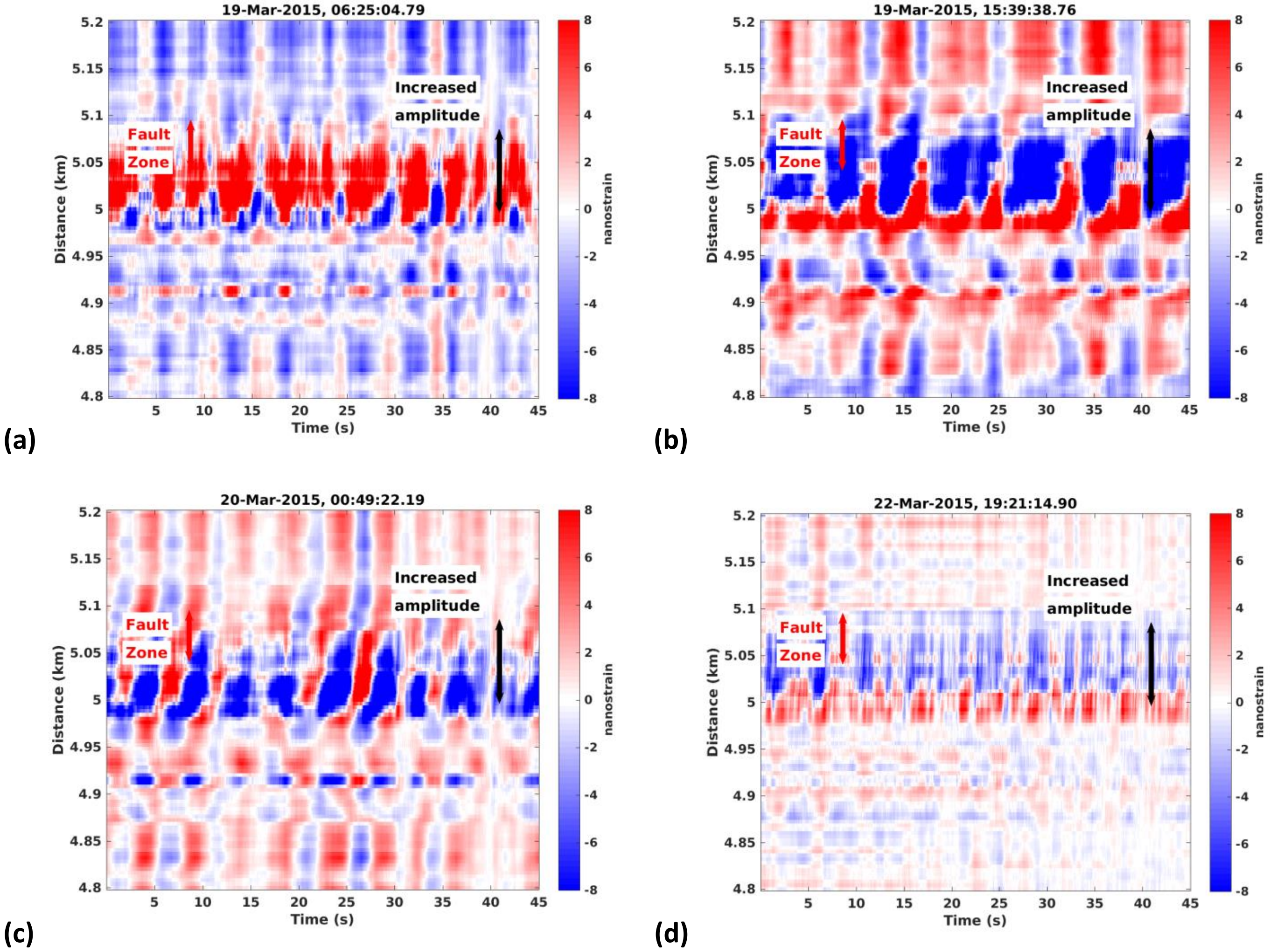

Supplementary Figure 9 | Examples of trapped micro-seism waves at various recording times (strain).

The fault zone visible at the surface in the field is indicated with the red double-arrow; the area with increased micro-seism amplitude is indicated by the black double-arrow. **a** 19 March 2015 06:25:4.79. **b** 18.03.2015 15:39:38.76. **c** 20.03.2015 00:49:22.19. **d** 22.03.2015 19:21:14.90

Supplementary References

1. Sigmundsson, F., Einarsson, P., Hjartardóttir, A.R., Drouin, V., Li, S., Jónsdottir, K., Árnadottir, T., Geirsson, H., Hreinsdóttir, S. & Ófeigsson, G. Geodynamics of Iceland and the Signatures of Plate Spreading. *Special Issue J. Volcanol. Geotherm. Res. – "Reykjanes*", **in press**.

2. Sigmarsson, O. & Steinthórsson, S. Origin of Icelandic basalts: a review of their petrology and geochemistry. *J. Geodynamics* **43**, 87-100 (2007).

3. Flovenz, Ó.G., & Saemundsson, K. Heat flow and geothermal processes in Iceland. *Tectonophysics* **225**, 123-138 (1993).

4. Clifton, A. E. & Schlische, R. W. Fracture populations on the Reykjanes Peninsula, Iceland: Comparison with experimental clay models of oblique rifting. *Journal of Geophysical Research* **108**, B2, 2074, doi:10.1029/2001JB000635 (2003).

5. Jumikis, A. R. Rock mechanics. *Trans. tech Publications*, Clausthal (1979).